

# JGR Space Physics

## TECHNICAL REPORTS: DATA

10.1029/2021JA029784

### Key Points:

- Plasma measurements in the solar wind from Magnetospheric MultiScale Mission's Fast Plasma Investigation (FPI) are compared with the OMNI solar wind database
- The electron density and ion velocity show good agreement with OMNI's proton density and velocity respectively
- The FPI ion density is underestimated and FPI ion temperature is overestimated when compared to OMNI

### Correspondence to:

O. W. Roberts,  
[owen.roberts@oeaw.ac.at](mailto:owen.roberts@oeaw.ac.at)

### Citation:

Roberts, O. W., Nakamura, R., Coffey, V. N., Gershman, D. J., Volwerk, M., Varsani, A., et al. (2021). A study of the solar wind ion and electron measurements from the magnetospheric multiscale mission's fast plasma investigation. *Journal of Geophysical Research: Space Physics*, 126, e2021JA029784. <https://doi.org/10.1029/2021JA029784>

Received 13 JUL 2021

Accepted 11 SEP 2021

## A Study of the Solar Wind Ion and Electron Measurements From the Magnetospheric Multiscale Mission's Fast Plasma Investigation

O. W. Roberts<sup>1</sup> , R. Nakamura<sup>1</sup> , V. N. Coffey<sup>2</sup> , D. J. Gershman<sup>3</sup> , M. Volwerk<sup>1</sup> , A. Varsani<sup>1</sup> , B. L. Giles<sup>3</sup> , J. C. Dorelli<sup>3</sup> , and C. Pollock<sup>4</sup> 

<sup>1</sup>Space Research Institute, Austrian Academy of Sciences, Graz, Austria, <sup>2</sup>NASA Marshall Space Flight Center, Huntsville, AL, USA, <sup>3</sup>NASA Goddard Space Flight Center, Greenbelt, MD, USA, <sup>4</sup>Denali Scientific, Fairbanks, AK, USA

**Abstract** We compare plasma measurements in the solar wind between the Magnetospheric MultiScale Mission's (MMS) Fast Plasma Investigation (FPI) and those obtained near the Earth-Sun L1 Lagrangian point from OMNI. FPI is an instrument designed to investigate plasma processes such as magnetic reconnection, acceleration, and turbulence. Since 2017, MMS supports solar wind campaigns where the plasma can have a higher Mach number, a cooler temperature, and a narrower beam compared with the MMS primary regions of interest. With FPI's firmware now optimized for these campaigns, the comparison with OMNI aids the interpretation of solar wind measurements. From these comparisons, we can make suggestions for both fast and burst-survey telemetry modes. From fast mode intervals, we find first, that the FPI ion density can be lower than the OMNI proton density. However, the FPI electron density agrees well with the OMNI proton density. Second, due to the solar wind's cooler proton temperature and narrow-angle, the FPI ion temperature is overestimated. Thus, using the OMNI proton temperature is suggested for plasma parameters such as the ion  $\beta$ , the ratio of ion thermal to magnetic pressure. Third, the FPI ion velocity is well-estimated when compared with the OMNI proton velocity. In burst mode, the ion density and temperature have similar characteristics but to a lesser degree. Spin effects observed in all these plasma moments in burst mode intervals are reduced with the methods discussed in this paper. The results are summarized in a table that includes linear fit parameters and their defined errors.

### 1. Introduction

The solar wind is a super Alfvénic flow of plasma emanating from the Sun and is the driver of various magnetosheath, magnetospheric and ionospheric phenomena. Characterizing the solar wind requires knowledge of plasma parameters such as the bulk speed, density, and temperature, along with the interplanetary magnetic field strength and orientation. Accurate knowledge of these parameters is vital to understand the solar wind's current state in addition to the transfer of its energy into the magnetosphere (Koskinen, 2002). Another example where accurate values of plasma parameters are essential is in the field of solar wind turbulence. Often utilized within this field as a diagnostic of the fluctuations is the Fourier power spectral density. At large scales a Kolmogorov-like inertial range is observed, followed by a break and a steepening near either; the ion inertial length  $d_i = v_A/\Omega_{ci}$ , the ion Larmor radius  $\rho_i = v_{th\perp i}/\Omega_{ci}$ , or the combined scale  $(\rho_i + d_i)$  (Bruno & Trenchi, 2014; Chen et al., 2014; Leamon et al., 1998; Markovskii et al., 2008). In these terms,  $\Omega_{ci}$  denotes the ion cyclotron frequency,  $v_A = B_0/\sqrt{\mu_0 n_i m_i}$  denotes the Alfvén speed, and  $v_{th\perp i}$  denotes the ion perpendicular thermal speed. The plasma parameters need to be known accurately to determine the relevant physical scale for the break in the spectrum.

The Magnetospheric MultiScale mission (Burch et al., 2016), launched in 2015, provides plasma and field measurements to investigate magnetic reconnection, particle acceleration, and turbulence. The Fast Plasma Investigation (FPI) (Pollock et al., 2016) along with other instruments provides the measurements for these and other magnetosheath-magnetospheric boundary processes. Since 2017, the orbit additionally carries the four spacecraft into the solar wind between November and May. Before launch, many decisions requiring trade-offs in instrument design are made for the final hardware to obtain the best measurements for the mission's science objectives. In-flight optimization of the instrument's firmware can then improve the

measurements obtained within a particular plasma regime. Previous studies have noted a discrepancy between values of the ion temperature measured by FPI when compared to the OMNI's Wind spacecraft (e.g., Bandyopadhyay et al., 2018; Burkholder & Otto, 2019; Bandyopadhyay et al., 2020; Chasapis et al., 2017; Roberts et al., 2020). Observations of the same discontinuity observed at THEMIS and at MMS also show a difference of ~ 30% for electron temperatures (Artemyev et al., 2019). These studies motivate a more detailed analysis of FPI's measurement limitations in the solar wind.

Compared to magnetospheric plasma, solar wind particle distributions are characterized by high flow velocity and are narrow in angle and temperature. Accounting for any uncertainties in this regime requires knowledge of the instrument's limitations and flight modes for the specific plasma region measurements. The Electrostatic Analyzer (McFadden, Carlson, Larson, Ludlam et al., 2008; McFadden et al., 2008a, 2008b) on the ARTEMIS (Angelopoulos, 2011) spacecraft has a similar design to FPI and, depending on the orbit, operates in a magnetospheric or solar wind mode. Artemyev et al. (2018) made a 6-year quantitative comparison of the solar wind plasma measurements between the ARTEMIS ESA and OMNI. Their onboard calculated ion and electron moments were used for this comparison. Here, we make quantitative comparisons between the solar wind measurements of OMNI and FPI's ground-processed moments to serve future solar wind studies.

The OMNI solar wind database, provided by specific spacecraft around the Sun-Earth L1 Lagrange point and time-shifted to the bow shock, is an ideal reference measurement for comparison (King & Papitashvili, 2005). This database consists of many plasma and field measurements, including proton density, proton velocity, and proton temperature, with the highest time resolution of 1 min. Since 2004, the two spacecraft primarily providing the measurements are the Advanced Composition Explorer (ACE) (Stone et al., 1998) and Wind (Harten et al., 1995; K. Ogilvie & Desch, 1997; Wilson III et al., 2021). The instruments of both spacecraft are designed for the plasma and field characteristics of the solar wind. The magnetic field and plasma data from Wind are measured by the Magnetic Field Investigation (MFI) (Lepping et al., 1995) and the Solar Wind Experiment (SWE) (K. W. Ogilvie et al., 1995), respectively. The SWE instrument design, optimized for Wind's solar wind orbit and mission objective, provides a valuable comparison to FPI's solar wind measurements.

## 2. Instrumentation

The FPI instrument consists of 16 Dual Ion Spectrometers (DIS) and 16 Dual Electron Spectrometers (DES) with each of the four spacecraft having four pairs. The instruments measure the three-dimensional velocity distribution functions (VDF) of ions and electrons, respectively. To obtain the corresponding macroscopic properties of the plasma, moments  $M$  of the VDF  $f(\vec{v})$  are taken (Baumjohann & Treumann, 1997; Gershman et al., 2015; Paschmann et al., 2000).

The zeroth order moment gives the number density  $n$

$$M_0 = n = \int f(\vec{v}) d^3 v \quad (1)$$

The first-order moment gives the flux density

$$M_1 = n\bar{v}_{bulk} = \int \vec{v}f(\vec{v})d^3 v \quad (2)$$

By dividing by the number density, the bulk velocity can be obtained. To distinguish between the bulk velocity and the particle velocities, we denote the bulk velocity as  $\bar{v}_{bulk}$ . The second-order moment yields the momentum flux density tensor.

$$M_2 = \Pi = m \int \vec{v}\vec{v}f(\vec{v})d^3 v \quad (3)$$

By subtracting the bulk velocity from the particle velocities as follows;

$$\mathbf{P} = m \int (\vec{v} - \bar{v}_{bulk})(\vec{v} - \bar{v}_{bulk})f(\vec{v})d^3 v \quad (4)$$

The momentum flux density  $M_2$  can be used to find the pressure tensor, where  $m$  is the particle mass, which is typically assumed to be the proton mass for DIS ion measurement. The pressure can then be used to obtain the temperature.

On each spacecraft, the FPI spectrometers are positioned at 90° intervals on the spacecraft body, providing an almost instantaneous view of the sky (termed all-sky) without completely relying on spacecraft spin for azimuthal coverage. Instantaneously, there are some small gaps in azimuth between detector heads; however, these are covered as the spacecraft rotates a small amount. The instruments operate continuously in burst mode with a VDF sampled each 0.15 s for ions and 0.03 s for electrons. Due to the telemetry challenges this creates, the science-regions-of-interest are downloaded primarily in an averaged fast-survey mode with a VDF obtained every 4.5 s. Specific measurements aligned with the mission's objectives or campaigns, such as solar wind intervals of interest, are selected by a scientist in the loop (SITL) and downloaded in burst mode resolution.

Primarily, the FPI measurements have an angular resolution of  $11.25^\circ \times 11.25^\circ$  using 16 simultaneous samples in the spacecraft's polar direction and 4 electrostatically swept deflections in the spacecraft's azimuthal direction. The energy range for the non-solar wind tables is either 2eV–19 keV or 2eV–30 keV for ions and 6eV–30 keV for electrons. This energy-azimuthal resolution can be too coarse for plasma characteristics in the solar wind, often characterized by cooler plasma temperatures or beams with a narrow angle. Note that typically the distributions of electrons are broader than the ions; therefore; the effects described here are more relevant for ion measurements. In the electrostatically swept azimuthal field of view, there can be gaps in the sampling of the plasma, causing spurious spacecraft phase angle dependent fluctuations in the burst mode data (e.g., Bandyopadhyay et al., 2018; FPI-Team, 2021). These manifest themselves as large spikes in the Fourier spectrum of the moment measurements. Therefore for solar wind measurements, FPI runs modified energy-azimuth tables. In these solar wind tables, FPI-DIS ion sampling has a revised angular resolution of  $11.25^\circ \times 5.625^\circ$  with eight versus the four regular azimuthal deflections and a revised energy range of 197–9,222 eV with a higher energy resolution to support the narrow and cooler solar wind. The FPI-DES's electron energy range is also modified to 4–940 eV with a higher energy resolution to support cooler electron temperatures in the solar wind (e.g., Wilson III et al., 2018). Even with these modifications for solar wind campaigns, vigilance is necessary when analyzing this plasma regime for accurate analysis.

### 3. IWF MMS Solar Wind Database

This paper's analysis uses the time intervals from the IWF (Institut für Weltraumforschung) MMS solar wind database (Roberts et al., 2020). These consist of 96 intervals of fast-survey mode data and 16 intervals of burst mode data in the solar wind from 2016 to 2020. In all of these intervals, the Active Spacecraft Potential Control (ASPOC) instrument (Torkar et al., 2016) was not operating. In the solar wind on MMS, the spacecraft potential is typically low  $\sim 4$  V. External photoelectrons (produced outside the instrument from the spacecraft body) are corrected by excluding energy channels that are below the spacecraft potential (e.g., Lavraud et al., 2016). The effects of internal photoelectrons (produced inside the instrument) are corrected using a model (Gershman et al., 2017). Both corrections are included in the ground processed moments of FPI. Therefore, we do not expect any significant spacecraft potential effects on the data. We use the data from the ground processed moment files from the MMS data archive. The data set is investigated by eye to ensure that there are no excursions, or only brief excursions into the foreshock where other processes such as backstreaming particles can affect the moments (e.g., Wilson III et al., 2014) and large amplitude waves are present (e.g., Turc et al., 2019). These effects at the foreshock prevent a direct comparison with the OMNI data at the Earth-Sun L1. The accepted intervals can be classified predominantly as the slow solar wind, consistent with 2016–2020 being in the declining phase of Solar Cycle 24 (Bhowmik & Nandy, 2018). The fast-survey mode intervals vary from 40 min in duration to many hours, with a mean of  $\sim 3$  hours, while the burst mode data are much shorter with a mean of  $\sim 46$  minutes. Figure 1 shows an example of one of the fast-survey mode intervals.

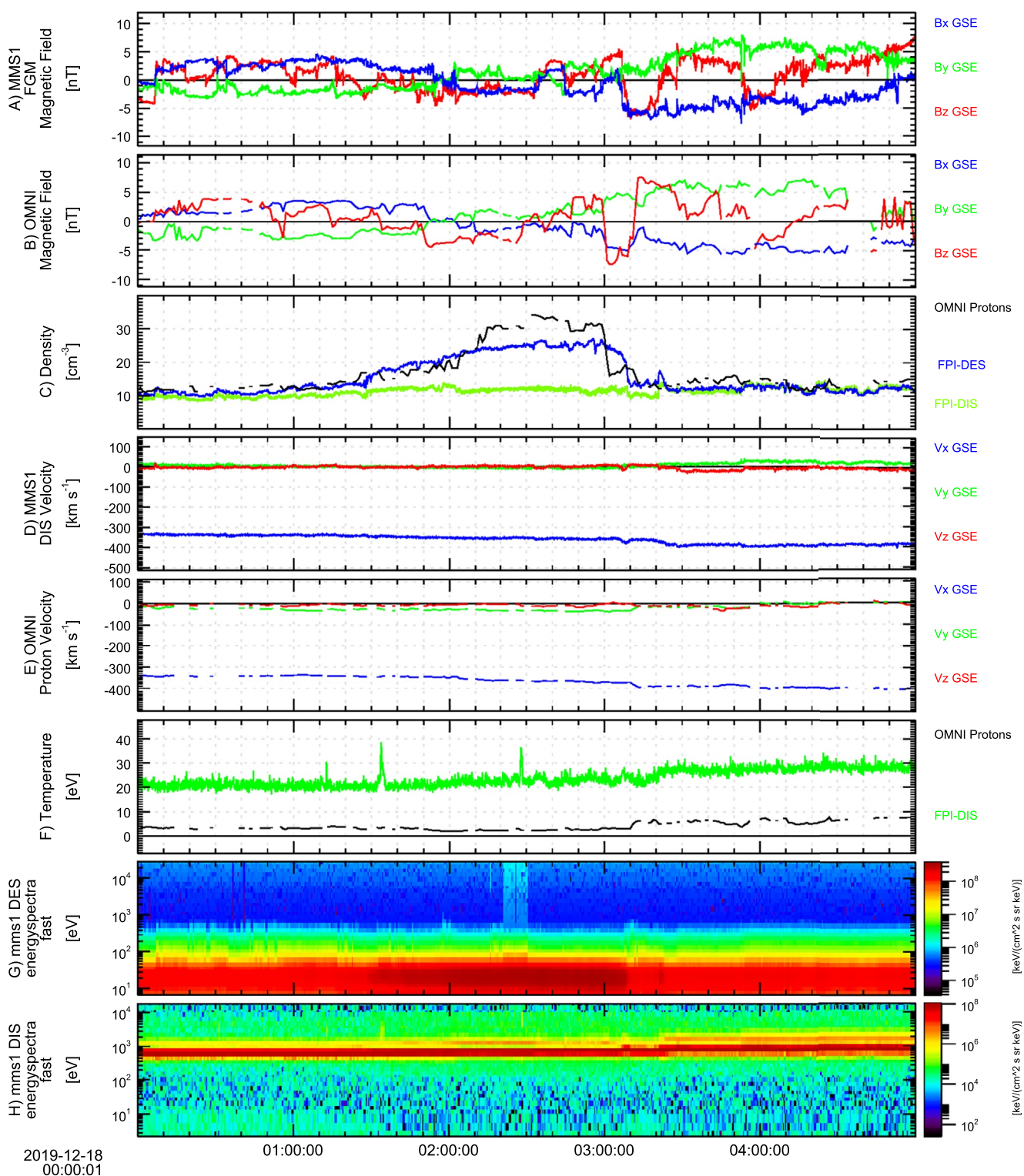


**Figure 1.** An overview of one event from the database, from top to bottom: (a) The MMS1 DC magnetic field components from the fluxgate magnetometer, (b) the OMNI DC magnetic field components, (c) densities including the OMNI proton density (black), the FPI electron density (blue), the FPI ion density (green), (d) the FPI ion velocity components, (e) the OMNI proton velocity components, and (f) The OMNI proton temperature (black) and FPI ion temperature (green), (g) the electron omnidirectional energy spectra from FPI-DES, and (h) the ion omnidirectional energy spectra from FPI-DIS. Note that the OMNI data in this case come from Wind.

Figure 1 illustrates a 5-h interval of solar wind measurements from the database on Dec 18, 2019, when FPI is not using a designated solar wind energy-azimuth table. The panels from top to bottom are: the magnetic field components from MMS1 FGM and OMNI, the OMNI proton and FPI electron and ion densities, the FPI ion velocity and OMNI proton velocity components, the OMNI proton and FPI ion temperatures, and the DES and DIS energy spectra. Qualitatively, the magnetic fields agree, although there is a difference of about 10 min most easily seen near 03:00 where the  $B_z$  components change sign. This difference is likely related to uncertainty in the OMNI time-shift to the bow shock and the relative location of the MMS spacecraft. During this interval, MMS1 and the Wind spacecraft are about 3 Re and 206 Re radially from the bow shock nose respectively. MMS is also not on the Sun-Earth line, which can introduce additional uncertainties (e.g., Vokhmyanin et al., 2019). Furthermore, the nominal bow shock location used in OMNI is determined from a model (Farris et al., 1994). Different models can yield different locations (e.g., Turc et al., 2013) and may be different to the true bow shock location. The FPI electron density and OMNI proton density show reasonable agreement for the majority of the interval. Near 01:30–03:10 UT, there is a strong enhancement in density observed in both the OMNI proton density and FPI's electron density that is not observed in the FPI ion density. Note that the FPI instrument measures ions with no mass per charge discrimination, while OMNI provides a proton measurement. The solar wind contains a small component of alpha-particles (~ 4% Alterman et al., 2019), which are also detected by the FPI ion measurement, and can affect the moment calculations. A mass per charge discriminated measurement is available on MMS from the Hot Plasma Composition Analyzer (HPCA) (Young et al., 2016), but due to its need to decimate the data to fit into the fast-survey telemetry, it is not included for comparison. Furthermore, HPCAs energy and angle resolution is not designed for solar wind measurements and so is not included in the burst-mode comparison either.

The observed density enhancement was likely due to a high speed solar wind stream linked to a coronal hole observed by NASA's Solar Dynamics Observatory and recorded in the online STAR catalog as CH947 ([https://www.solen.info/solar/coronal\\_holes.html](https://www.solen.info/solar/coronal_holes.html)). Throughout this interval, the error flags (not shown) for the electron measurement denote a significant (> 25% of the total) cold component not detected by the instrument, indicating an underestimated density. The FPI ion measurement has two error flags (not shown), one indicating that the ion instrument is either saturated or over-counting (when the counts in a bin exceed  $2^{16}$ , however with compression this value is closer to ~ 60,000), and the other error flag indicating a high sonic Mach number (i.e., when  $M_s > 2.5$ .) Saturation refers to the scenario in which the detector is not able to respond to high incident fluxes i.e., the instrument under responds. Over-counting refers to the scenario where the pixel counter has reached its maximum. Here, we refer to pixel counter as the accumulated number of digital counts from a single pre-amplifier channel. The instruments operate continuously in burst mode during science regions of interest, with the fast-survey mode data obtained by averaging the burst mode data. In other words, the instrument sums the total number of counts in any given energy-angle bin on board and accumulation times are adjusted on ground accordingly. However, the maximum number of counts for a pixel is the same for both fast-survey and burst modes. If the maximum number of counts is reached then the average will be underestimated and over-counting occurs. In Figure 1, we see over-counting becomes prevalent for densities  $> 10\text{cm}^{-3}$  in the ion data where  $n_i$  deviates from  $n_e$ . With the shorter integration time in burst mode, the ion measurements are more robust to over-counting effects; however, saturation can still affect burst mode. Effectively in burst mode, saturation will occur before over-counting. The OMNI proton velocities and FPI ion velocities agree well. Between the OMNI proton and FPI ion temperature, there is an approximate factor of 4 between the two derived measurements that will be discussed further.

To ensure that comparisons between OMNI ion data and MMS plasma data are possible for these intervals, we first compare the magnetic field measurements from the fluxgate magnetometers (Russell et al., 2016) on MMS1 to the OMNI data. With the MMS magnetic field measurements sampled at 16 Hz in fast survey mode, 128 Hz in burst mode, and the OMNI low-resolution data at 0.0167 Hz (1-min cadence), we used time averages over the entire interval to overcome the uncertainty in the OMNI data's time shift as is seen in Figure 1. The comparison of the magnetic field components in the Geocentric Solar Ecliptic (GSE) coordinate system is presented in Figure 2 for fast survey mode intervals and in Figure 3 for all the burst mode

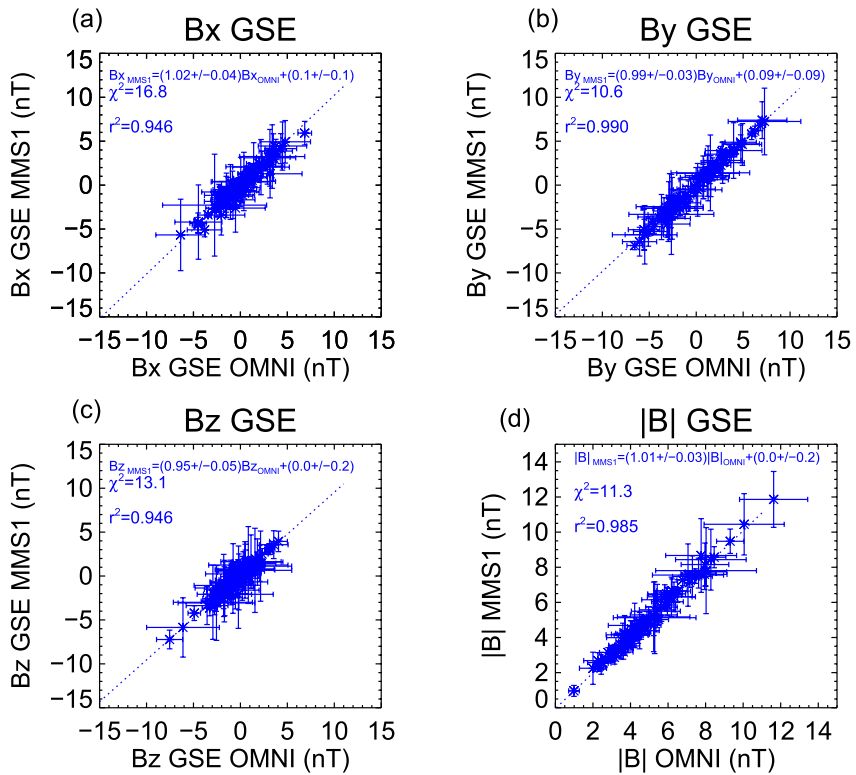


**Figure 2.** Comparison of the magnetic field components between OMNI and MMS1 (a)–(c), and the comparison of the magnetic field's magnitude (d). The points denote the mean value in the interval, while the error bars denote the sample standard deviation. The fitted parameters and their errors are indicated on the plot. The values of the  $\chi^2$  (goodness-of-fit measure) and the  $r^2$  (a measure of the how much of the data variability the model describes) are also indicated.

intervals. The points denote the mean of the measurements in the interval, and the error bars denote the sample standard deviation of the measurements. The mean is used rather than the median as measured quantities in the solar wind (e.g., magnetic field) have Gaussian distributions (Padhye et al., 2001). The linear fit to the data is determined from a linear least squares approximation. The linear fit is denoted by the dotted blue line and is shown along with its fitted intercept and slope. Also given is the  $\chi^2$ , a measure quantifying the goodness of the fit, and the coefficient of determination,  $r^2$ , describing how much of the variance of the MMS observations is explained by the linear fit. The slopes and the  $r^2$  are near 1, indicating a good match. The excellent agreement between the MMS1 and OMNI magnetic field measurements for both fast survey mode and burst mode gives us the confidence that the approach pursued here is appropriate. We now describe some of the properties of the FPI instrument.

#### 4. FPI Versus OMNI Comparisons

##### 4.1. Fast Survey Mode

We now focus on comparing OMNI with FPI's ground-processed moments from in fast-survey mode when utilizing the solar-wind and non-solar wind flight tables. For this comparison, we use the solar wind intervals detailed in (Roberts et al., 2020), which occur between 2016 and 2020, and separate them into times where the solar wind energy-azimuth table is in use and when it is not. Assuming quasi-neutrality ( $n_i = n_e$ ), we compare the OMNI proton density to both the FPI ion density and the FPI electron density in the following two figures. As was done similarly to the magnetic field data analysis in Figures 2 and 3, we compare time averages of OMNI and MMS1 over the entire interval to avoid uncertainties in the time-shifting of the OMNI data. Since the FPI ion density is without mass discrimination, the FPI ion data is indicated with a subscript  $i$ . The OMNI provides a proton density

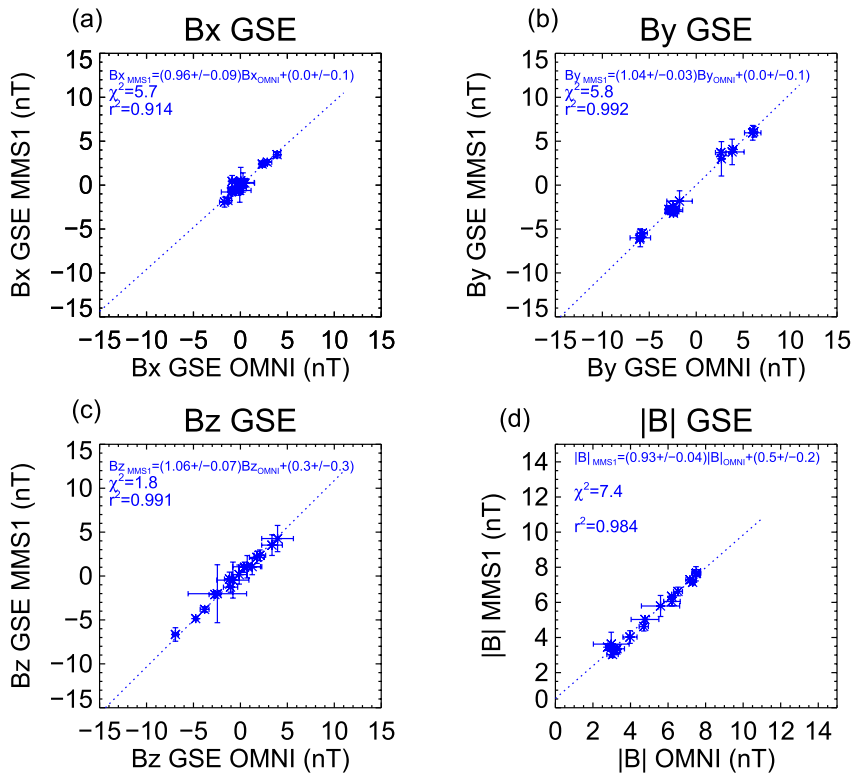


**Figure 3.** Shows the same as Figure 2 but for the burst mode intervals.

and is indicated with a subscript  $p$ . In these figures, FPI data using the solar wind energy-azimuth table are in blue, and the data using the non-solar solar wind table are in red. All the figures in this paper will use this convention in differentiating the data between the solar wind and non-solar wind tables. Shown within these figures is the linear regression fits with their standard errors. Provided also is the  $\chi^2$  goodness of fit measure and the  $r^2$  coefficient of determination, a measure of how well the linear regression predicts the OMNI data.

Figure 4a compares the FPI ion density from fast-survey mode with the OMNI proton density. These data show that the FPI density with both the solar wind and non-solar wind tables is underestimated with slopes of 0.52 and 0.62, respectively. This density starts to deviate from the OMNI proton density near  $10 \text{ cm}^{-3}$  as seen in Figure 1c, flattening as the OMNI density increases. This flattening is likely due to over-counting with all particle counts within a few pixels.

As can be seen in the DIS ion energy spectra in Figure 1h, the solar wind's cooler temperature (and often its narrow angle) can cause a concentration of high counts in a small number of energy steps over a small number of polar pixels. As the fast-survey mode averages the 30 summed burst all-sky maps (for ions), it will begin over-counting if the counts reach the maximum allowed. Should a pixel reach the maximum counts of the detector, the zeroth-order density moment in Equation 1 will be under-estimated. Data affected by this are given a bit-1 error flag denoting that either saturation or over-counting effects may be present. This feature can be more prevalent in the fast-survey data because both the fast and burst survey modes have the same maximum number of counts in a pixel.

Figure 4b compares the electron density with the OMNI proton density. Although the electron data can also become saturated for values  $> 25 \text{ cm}^{-3}$ , such high densities are not typical for quiescent solar wind even though they can occur during transient events such as the event on December 18, 2019. The FPI electron density agrees better (compared to the ion density) with the OMNI proton density in terms of the slope of

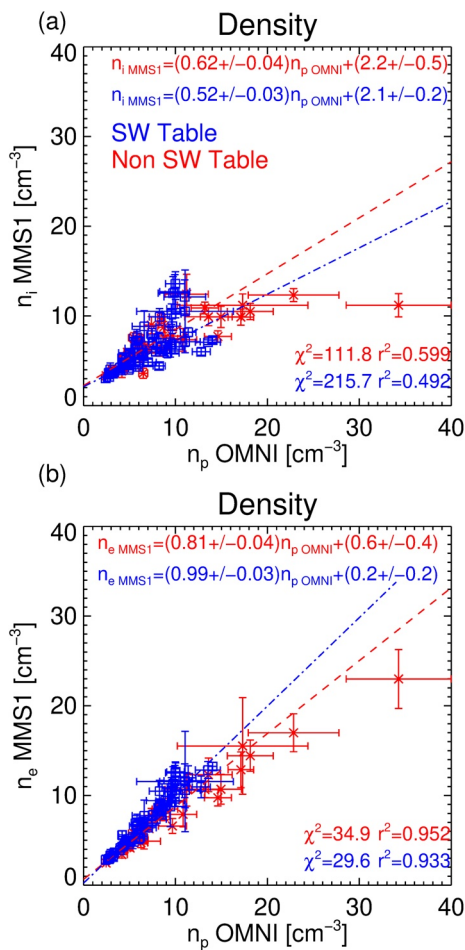


**Figure 4.** Comparison of the OMNI proton density with the FPI densities in fast-survey mode. (a) Comparison with FPI ion density and (b) comparison with FPI electron density.

the linear fit, a reduced intercept, and  $\chi^2$  and a larger  $r^2$ . A challenge specifically for electron measurements is that the instrument also detects photoelectrons both from the spacecraft and internal to the instrument (Gershman et al., 2017). Nevertheless, a model is provided on the MMS data archive to remove this photoelectron contribution. As with the ions, there can also be a lower energy component to the electron distribution, which is not measurable due to contamination from low energy spacecraft external photoelectrons. In the solar wind, the spacecraft potential is typically low and positive with minimal effects.

A detailed comparison between the ion density provided by DIS and the electron density provided by DES in fast-survey mode is shown in Figure 5. As there is no time shift to consider, no averaging needs to be performed, yielding many more data points. The total number of data points is 251,502, with ~70% using the solar wind table and ~30% using the non-solar wind table. Figure 5a shows the entire data set while 5b and 5c shows the data obtained with the non-solar wind and solar wind table respectively. Similarly to Figure 4a, we see regions where the ion density is saturated. This is most notable in the data with the non-solar wind table (b), where near  $n_i = 10 \text{ cm}^{-3}$  there is a strong deviation from the  $n_i = n_e$  line. This feature is also present in the data using the solar wind table (c) but is less severe.

Shown in Figure 6 is the comparison between the FPI ion and OMNI proton velocity components in the GSE coordinate system. The bulk velocity is expected to be accurate as the first-order moment would not be as affected by over-counting/saturation. In other words, the mean value of the distribution would be similar, unless a large number of pixels are saturated. As solar wind velocity is predominantly in the negative x-direction, there is very little difference between the quality of the regression for the  $V_x$  component and the magnitude of the three components from OMNI IV. Both the  $V_x$  component and the magnitude of the velocity IV show excellent agreement with the OMNI data for both solar and non-solar wind energy-azimuth tables.

The  $V_y$  component shows an interesting feature in Figure 6b where the data obtained with the non-solar wind table is larger than that obtained with the solar wind table, with the two populations well separated.

This separation results in a much larger value of the intercept which is  $29 \text{ km s}^{-1}$  for the non-solar wind table versus  $10.7 \text{ km s}^{-1}$  for the solar wind table. This is potentially caused by the coarseness of the non-solar wind table, which causes the increment in velocity  $\Delta V$  measured by the instrument to be larger. As the measurement in  $V_x$  is larger than  $V_y$ , the uncertainty due to this effect is much smaller in relative terms in  $V_x$  despite being the same in absolute terms. This feature could also be due to the additional FPI He+ within its ion measurement along with the less resolved energy and azimuth angle range. For the  $V_z$  component, the data from both flight tables are comparable and agree well with the OMNI data.

As discussed earlier, the optimized FPI table is more suitable for solar wind measurements in terms of both energy and angle range and their resolution. Higher-order moments providing the average plasma temperature are expected to be affected due to the combination of low energy-azimuth angle resolution compared to the beam size and temperature and a possible flatter distribution due to over-counting/saturation effects. Figure 7 shows the comparison between the OMNI proton temperature and the FPI ion temperature from fast-survey mode. The fitting coefficients indicate that the FPI ion temperature with its optimized solar wind table has an improved correlation as compared to the non-solar wind table. As similarly stated in Artemyev et al. (2018), there are still two main effects responsible for FPI's over-estimation of this temperature with the optimized table. For a beam with a  $V_x$  solar wind velocity range of  $300\text{--}600 \text{ km s}^{-1}$  ( $470\text{--}1,880 \text{ eV}$ ),

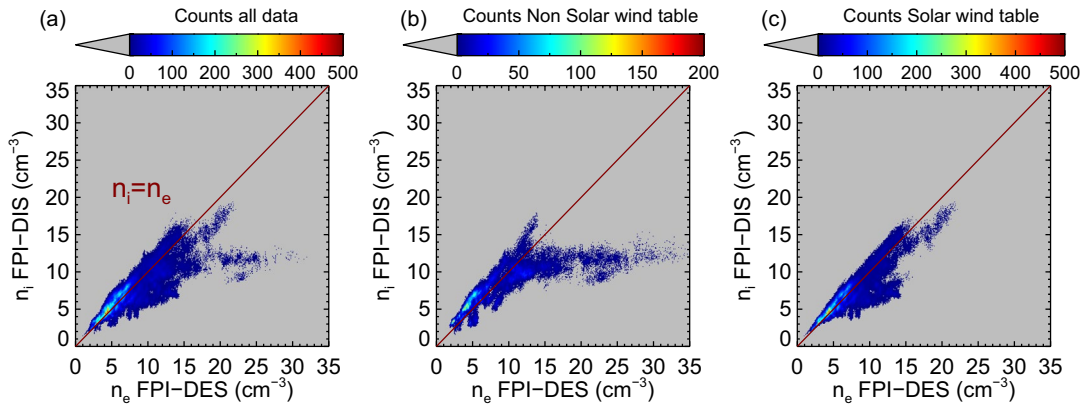


**Figure 5.** Two-dimensional histograms showing the relationship between the FPI ion density and electron density with (a) the entire data set, (b) the data with the non-solar wind table, and (c) the data with the solar wind table. The red line denotes the relation  $n_i = n_e$ .

the designed DIS energy bandpass would measure temperatures of approximately 56–225 eV. For reference, Wilson III et al. (2018) state a mean solar wind temperature of 12.7 eV. With the increased angular resolution of the solar wind table, a measured perpendicular beam temperature could possibly be resolved. Second, FPI's measurements do not separate ion species, and so helium ions, having a mass to charge ratio of 2, are counted as protons and so form a high-energy tail of the measured ion distribution function, effectively increasing the measured temperature [e.g., Halekas et al. (2014)].

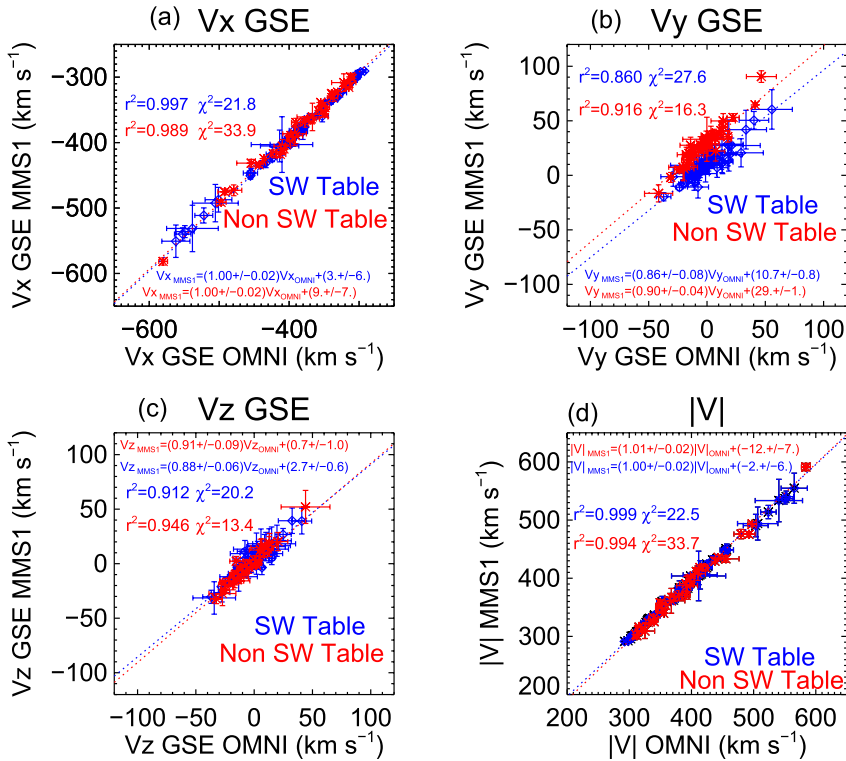


**Figure 6.** The relationship between OMNI proton velocities and MMS1 FPI ion velocities in fast-survey mode.

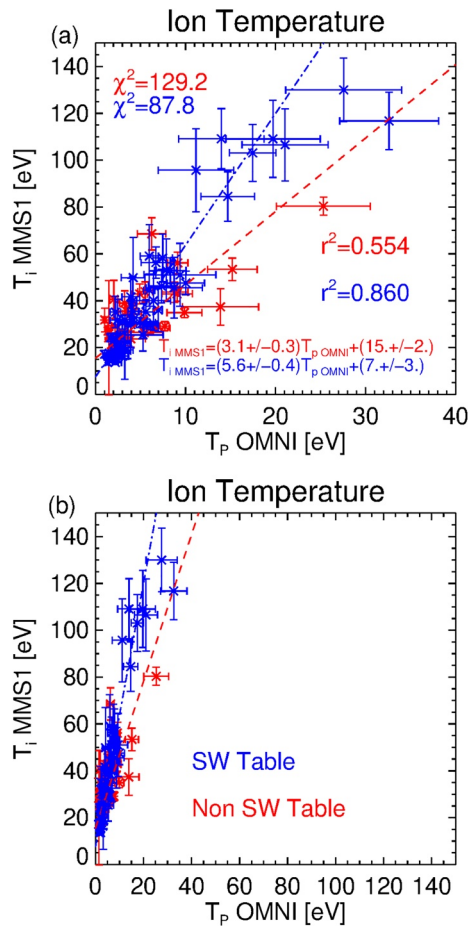


**Figure 7.** The relationship between the OMNI proton temperature and the MMS1 FPI ion temperature in fast-survey mode. (a) shows the data with a smaller  $x$  axis so the points can be seen in more detail, and (b) shows the same data where both axes are equal.

#### 4.2. Burst Survey Mode

In this section, we discuss the limitations of FPI burst mode data for solar wind measurements. If a VDF has a narrower beam compared to the angular resolution, there will be gaps in the plasma samples as the spacecraft phase angle changes. This effect can lead to a sharp angular structure in the measurements and large spin tones (MMS FPI Data Users and Products Guide, FPI-Team, 2021). If the user wishes to use the full burst mode resolution data, the spin tone should be removed before analysis. Below, we discuss the method we use to remove the spin effects in the burst mode data. After the spin removal, we compare the FPI with the OMNI data. We first illustrate the spin effects using the burst mode data on November 24, 2017, between 01:10:03–02:10:03 UT on MMS1 obtained with the solar wind table. The fluctuations, defined by subtracting the mean of the interval, of several plasma moments as a function of the spacecraft phase angle, are shown in Figure 8. The mean value after binning the data into  $0.5^\circ$  bins is shown in red. The mean value removed to give the fluctuations is stated on the right. The ion density in Figure 8a shows large fluctuations with respect to the mean value of the interval. Furthermore, there is a variation, indicated by the blue vertical lines, occurring every  $90^\circ$ , at  $\sim [30, 120, 210, 300]^\circ$  at the spin phase angles of FPI's four instrument heads. In contrast, the fluctuations in electron density (Figure 8b and on a different scale) are much smaller than the mean value. The velocity components (Figures 8c–8e) also show spin effects. The variation in relation to the mean is small for the  $V_x$  and  $V_z$  components but is comparable for  $V_y$ . However, the mean of the three velocity components are expected to be accurate, since their variation is centered near zero, with

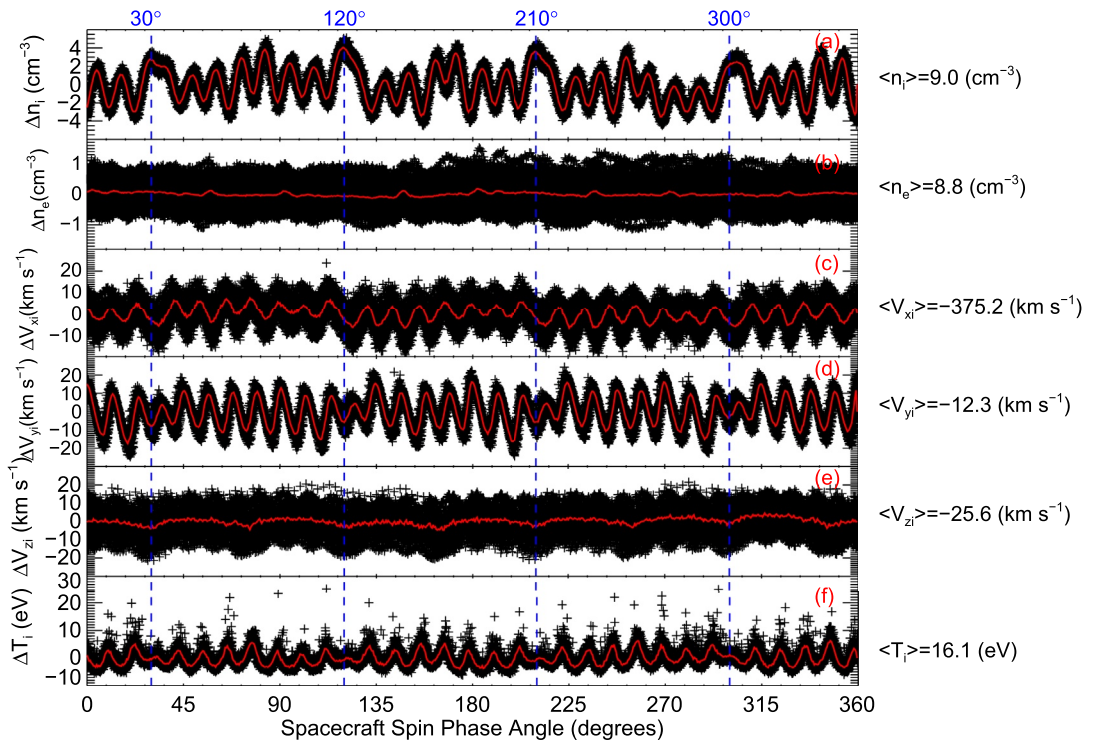


**Figure 8.** The relationship between the fluctuations ( $\Delta n_i = n_i - \langle n_i \rangle_i$ ) of measured plasma parameters with spacecraft phase angle for a burst mode interval of solar wind from MMS1 on November 24, 2017 between 01:10:03 and 02:10:03 UT. (a) Ion density, (b) electron density, (c)–(e) the components of velocity, and (f) the ion temperature. The blue dashed lines denote the pointing direction of the FPI four heads on the spacecraft. The red lines denote the averages based on binning the data in half-degree bins. The mean value subtracted from each parameter is indicated on the right.

the spin effects averaging out. Should averages be taken over time scales smaller than the spin period there may be some effects that need to be corrected. Figure 8f shows the fluctuations in the ion temperature, where the spin variation is also comparable to the mean and varies differently, with larger peaks above zero than below zero. If the user wants to use the data in a point to point manner, then some pre-processing is recommended. In Bandyopadhyay et al. (2018), this was done by using special implementation of a Hampel filter. Typically, Hampel filtering is used in the time domain, with the local median calculated using a sliding window. Any points larger than an established threshold are removed and replaced by the median in the window. However, in Bandyopadhyay et al. (2018), the Hampel filter was applied in frequency space to remove the spin spikes in the power spectrum. Then, the time series is recovered without the spin fluctuations by using the inverse Fourier transform. We now present a different method to remove the spikes based on an empirical model of the angular response of the detector.

To correct for the spin tones, we use a method previously used to remove spin tones from spacecraft potential (Roberts et al., 2017). An empirical model of the detector response as a function of the spacecraft phase angle is obtained from the data as follows; The fluctuations are binned (red lines in Figure 8), and a model  $M(\theta)$  is fitted to the binned data. Here, the model is a superposition of Gaussian functions. After the model has been derived, the spin corrected data  $D_{corr}(\theta)$  can be obtained from the original data  $D(\theta)$  following;  $D_{corr}(\theta) = D(\theta) - M(\theta)$ . The fitted models are shown in blue and the mean data in each bin are shown in red in Figure 9.

Figure 10 shows the power spectral densities of the data from the moment files in black and the corrected data using the method described above in red. The spikes at the spin tones (0.05 Hz and higher harmonics) have been removed or significantly reduced. Between 1 and 2 Hz, there is a peak in  $n_i$ ,  $V_x$ ,  $V_y$ . There are no

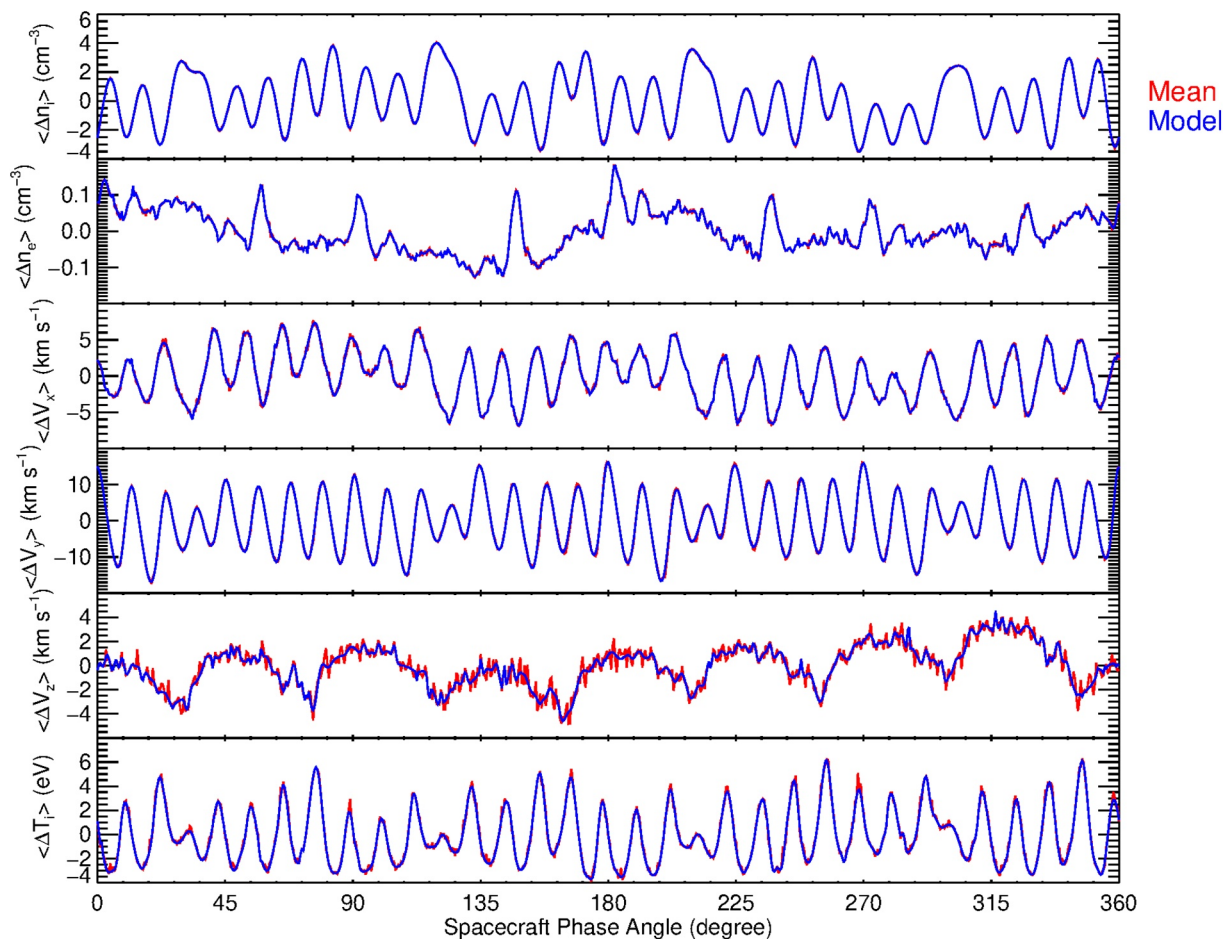


**Figure 9.** The mean fluctuations are shown in red which correspond to the red lines in Figure 8. The fitted model is shown in blue. This figure has the same format as Figure 8.

corresponding peaks in the magnetic field (Figures 10g and 10h), which suggests that these fluctuations are not due to wave activity e.g., magnetosonic waves.

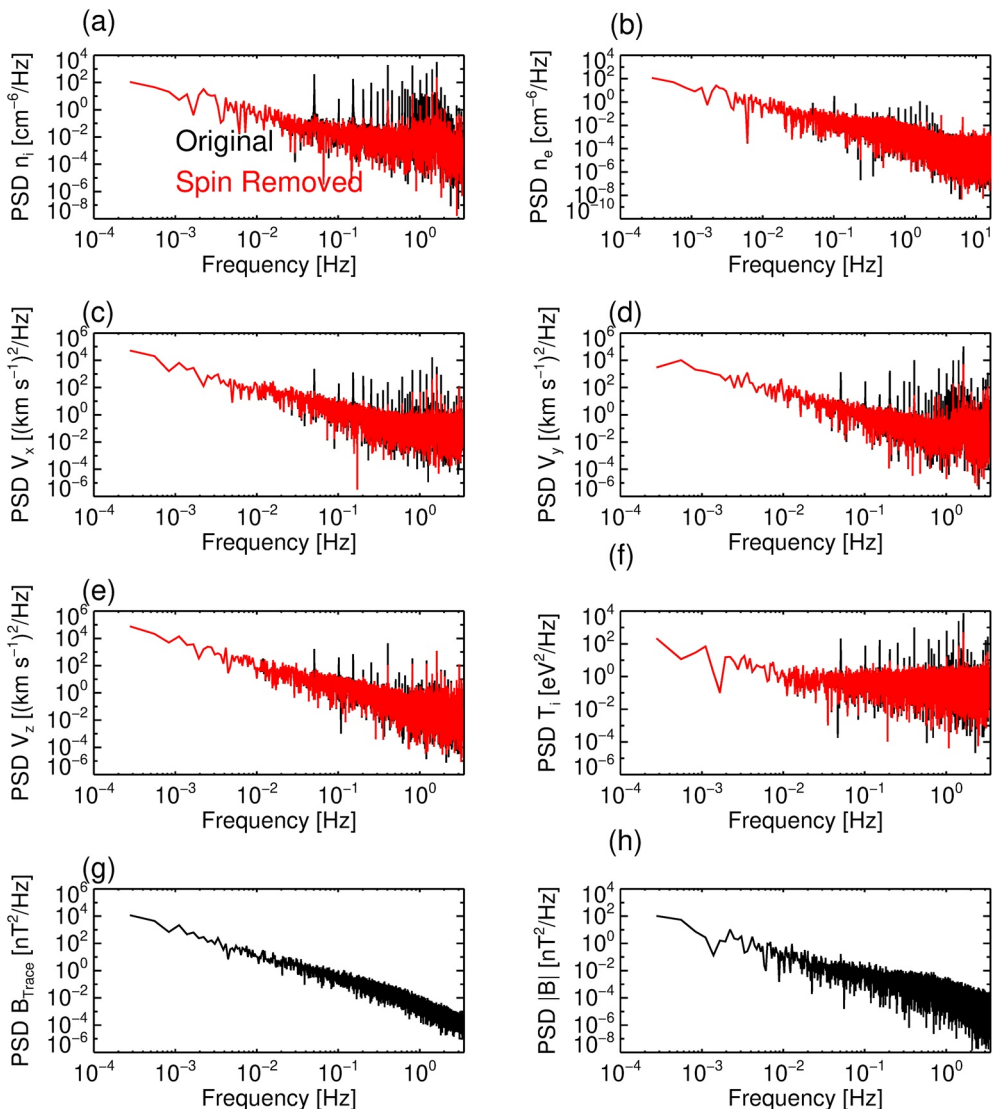
We now repeat the comparison of FPI data from burst mode with OMNI data as was done in fast-survey mode. In the ion density comparison shown in Figure 11, we see the density is somewhat underestimated, similar to that seen in the fast-survey mode. However, the electron density shows excellent agreement with the OMNI proton density.

Figure 12 shows the comparison of the OMNI proton and FPI ion velocities from the burst mode intervals. These are showing good agreement as was also seen in fast-survey.

The comparison of the OMNI proton temperature with the FPI ion temperature from burst mode intervals is shown in Figure 13. While there is still a significant offset, for the solar wind table, the slope is closer to one, and there is a linear relation; however, for burst mode, there are very few data points.

## 5. Summary

We have investigated the plasma measurements from MMS FPI in the solar wind as was similarly done by Artemyev et al. (2018) for ARTEMIS. We compare the solar wind data from FPI's fast and burst survey modes with the OMNI 1-min measurements obtained near the Earth-Sun L1 Lagrangian and time-shifted



**Figure 10.** Power spectral densities of the measured moments (black) and those that have been corrected for spin (red). The PSDs for the (a) ion density, (b) electron density, (c)  $V_x$ , (d)  $V_y$ , (e)  $V_z$  components of velocity, and (f) the ion temperature are shown. For context, the trace magnetic (g) and the magnetic field magnitude (h) are also shown.

to the bowshock nose. The dates and times utilized for this comparison study are from the IWF solar wind database used in other published studies.

Within this database, the FPI energy-azimuth table was not always optimized for solar wind measurements since its commissioning. Therefore, the OMNI data's correlations are with two FPI tables: the solar wind table and the table used in the remaining MMS orbit. The optimized FPI energy-azimuth table improves the agreement with the OMNI data but still necessitates understanding FPI's derived moments before applying them in a solar wind study. Described below are the final details. The results from the linear regression for fast and burst survey mode for the solar wind and non-solar wind energy-azimuth flight tables are summarized in Table 1. The table displays the slopes and intercepts obtained from linear regression, their standard errors, as well as the  $r^2$  value. For the majority of the measured parameters the solar wind table gives better performance in terms of a slope close to 1 and a smaller intercept, while in the majority of cases the  $r^2$  values between both tables are comparable.

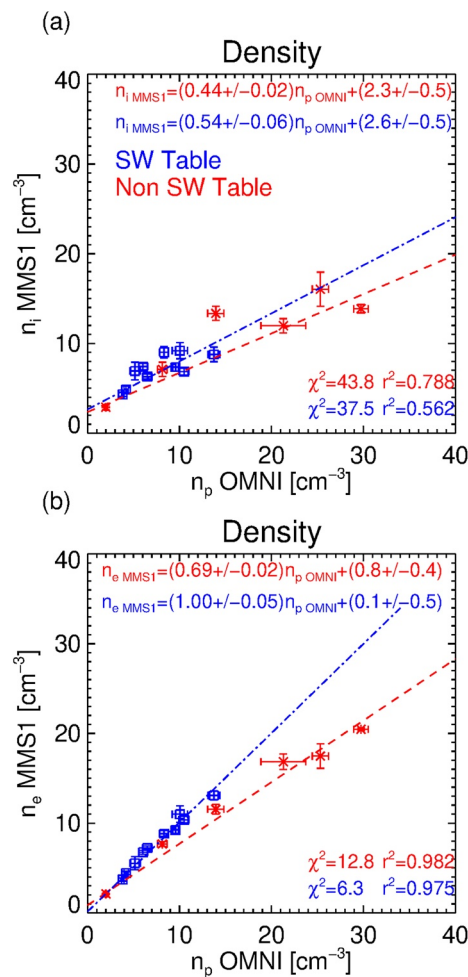


**Figure 11.** Comparison of the OMNI proton density with the FPI densities in burst mode (a) comparison with FPI ion density and (b) comparison with FPI electron density. Same as Figure 4 but for the burst mode intervals.

Comparing to the OMNI proton density, the FPI electron density agrees well and can be used for solar wind densities if quasi-neutrality is assumed. However, it can still be under-estimated for large atypical solar wind densities. Additionally, electron measurements can be subjected to effects from the spacecraft potential but is minimal. Comparing to the OMNI proton density, the underestimation of the FPI ion density caused by overcounting or saturation is improved in both the fast-survey and burst-mode data in the solar wind energy-azimuth table.

The OMNI proton velocity and FPI ion velocity agree well. Even if a pixel counter is over-counting or saturated, the distribution's peak will be at the correct energy. Additionally, the offset observed in the ion  $V_y$  velocity is improved with the solar wind energy-azimuth table.

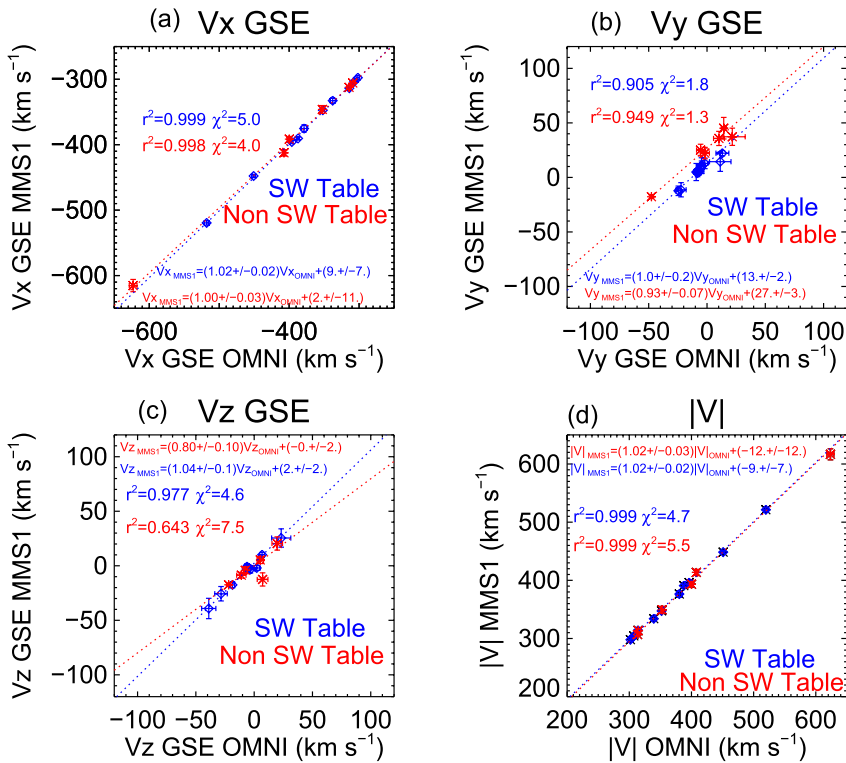


**Figure 12.** The relationship between OMNI proton velocities and MMS1 FPI ion velocities in burst mode. This figure follows the same format as Figure 6 but is for the burst mode intervals.

Comparing to the OMNI proton temperature, the FPI ion temperature with the solar wind table has better agreement but still over-estimated. The solar wind proton temperature is primarily cooler and sometimes narrower in angle than the FPI DIS hardware designed energy resolution. Additionally, helium ions measured by FPI can add a tail to its non-mass discriminated ion distribution, effectively making the temperature broader. The OMNI proton temperature can be used to calculate parameters such as the ion plasma  $\beta$  (the dimensionless ratio of ion thermal to magnetic pressure) (Bandyopadhyay et al., 2018, 2020; Chasapis et al., 2017; Roberts et al., 2020).

To summarize, the plasma moments from FPI in the solar wind are still subject to some limitations and should be used carefully. In many cases, the electron density is a good approximation for the solar wind density. The velocity components are accurate with spin tone removal. The OMNI proton temperature can be used to calculate parameters such as ion plasma  $\beta$ . Our study provides further justification and details for using the electron number density (as opposed to the ion density) in the solar wind, and OMNI for a measurement of the proton temperature and other derived parameters as was done by Chasapis et al. (2017), Roberts et al. (2020).

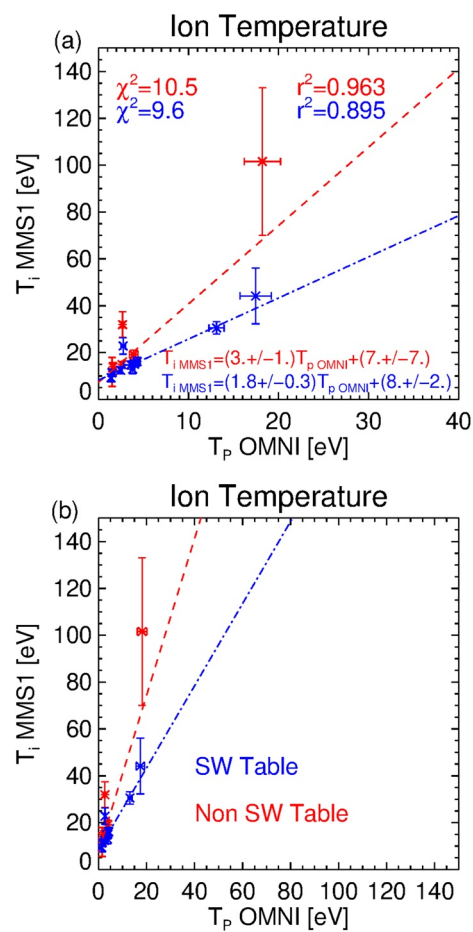


**Figure 13.** The relationship between the OMNI proton temperature and FPI ion temperature in burst mode. This figure follows the same format as Figure 7 but is for the burst mode intervals.

**Table 1**

Slopes and Intercepts Obtained From Regression (and Their Standard Errors Coming From the Residuals of the Fits) and  $r^2$  Values

	Slope		Intercept		$r^2$	
	SW	N-SW	SW	N-SW	SW	N-SW
<b>Fast survey mode</b>						
$n_i$	$0.52 \pm 0.03$	$0.62 \pm 0.04$	$2.1 \pm 0.2$	$2.2 \pm 0.5$	0.492	0.599
$n_e$	$0.99 \pm 0.03$	$0.81 \pm 0.04$	$0.2 \pm 0.2$	$0.6 \pm 0.4$	0.933	0.952
$M$	$1.00 \pm 0.02$	$1.01 \pm 0.02$	$2 \pm 6$	$12 \pm 7$	0.999	0.994
$V_x$	$1.00 \pm 0.02$	$1.00 \pm 0.02$	$3 \pm 6$	$9 \pm 7$	0.997	0.989
$V_y$	$0.86 \pm 0.08$	$0.90 \pm 0.04$	$10.7 \pm 0.8$	$29 \pm 1$	0.860	0.916
$V_z$	$0.88 \pm 0.06$	$0.91 \pm 0.09$	$2.7 \pm 0.6$	$0.7 \pm 1.0$	0.912	0.946
$T_i$	$5.6 \pm 0.4$	$3.1 \pm 0.3$	$7 \pm 3$	$15 \pm 2$	0.860	0.554
<b>Burst survey mode</b>						
$n_i$	$0.54 \pm 0.06$	$0.44 \pm 0.02$	$2.6 \pm 0.5$	$2.3 \pm 0.5$	0.562	0.788
$n_e$	$1.00 \pm 0.05$	$0.69 \pm 0.02$	$0.1 \pm 0.5$	$0.8 \pm 0.4$	0.975	0.982
$M$	$1.02 \pm 0.02$	$1.02 \pm 0.03$	$9 \pm 7$	$12 \pm 12$	0.999	0.999
$V_x$	$1.02 \pm 0.02$	$1.00 \pm 0.03$	$9 \pm 7$	$2 \pm 11$	0.999	0.998
$V_y$	$1.0 \pm 0.2$	$0.93 \pm 0.07$	$13 \pm 2$	$27 \pm 3$	0.905	0.949
$V_z$	$1.04 \pm 0.10$	$0.80 \pm 0.10$	$2 \pm 2$	$0 \pm 2$	0.977	0.643
$T_i$	$1.8 \pm 0.3$	$3. \pm 1.$	$8 \pm 2$	$7 \pm 7$	0.895	0.963

Note. SW denotes the solar wind energy-azimuth table, and N-SW denotes the non-solar wind energy-azimuth table.

## Data Availability Statement

The Magnetospheric MultiScale mission data are available from <https://lasp.colorado.edu/mms/sdc/public/>. Details of the intervals analyzed in this study can be seen in Roberts et al. (2020).

## Acknowledgments

Analysis of MMS data is partially supported by Austrian FFG projects ASAP15/873685. RN was supported by Austrian FWF projects I2016-N20. The authors acknowledge the FPI team and the other MMS instrument teams which made this study possible. OWR and VC acknowledge helpful discussions with the FPI team and with Mike Chandler regarding FPI. OWR and VC also acknowledge helpful discussions with Stephen Fuselier regarding HPCA. OWR also acknowledges helpful discussions with Natalia Papitashvili. We acknowledge use of NASA/GSFC's Space Physics Data Facility's OMNIWeb service and OMNI data.

## References

- Alerman, B. L., & Kasper, J. C. (2019). Helium variation across two solar cycles reveals a speed-dependent phase lag. *The Astrophysical Journal Letters*, 879(L6). <https://doi.org/10.3847/2041-8213/ab2391>
- Angelopoulos, V. (2011). The ARTEMIS mission. *Space Science Reviews*, 165(1–4), 3–25. <https://doi.org/10.1007/s11214-010-9687-2>
- Artemyev, A. V., Angelopoulos, V., & McTiernan, J. M. (2018). Near-earth solar wind: Plasma characteristics from ARTEMIS measurements. *Journal of Geophysical Research: Space Physics*, 123(12), 9955–9962. <https://doi.org/10.1029/2018JA025904>
- Artemyev, A. V., Angelopoulos, V., Vasko, I. Y., Runov, A., Avanov, L. A., Giles, B. L., et al. (2019). On the kinetic nature of solar wind discontinuities. *Geophysical Research Letters*, 46, 1185–1194. <https://doi.org/10.1029/2018GL079906>
- Bandyopadhyay, R., Chasapis, A., Chhiber, R., Parashar, T. N., Maruca, B. A., Matthaeus, W. H., et al. (2018). Solar wind turbulence studies using MMS fast plasma investigation data. *The Astrophysical Journal*, 866(2), 81. <https://doi.org/10.3847/1538-4357/aade93>
- Bandyopadhyay, R., Matthaeus, W. H., Chasapis, A., Russell, C. T., Strangeway, R. J., Torbert, R. B., et al. (2020). Direct Measurement of the solar-wind Taylor microscale using MMS turbulence campaign data. *The Astrophysical Journal*, 899(1), 63. <https://doi.org/10.3847/1538-4357/ab9ebe>
- Baumjohann, W., & Treumann, R. (1997). *Basic space plasma physics*. London: Imperial College Press.
- Bhowmik, P., & Nandy, D. (2018). Prediction of the strength and timing of sunspot cycle 25 reveal decadal-scale space environmental conditions. *Nature Communications*, 9(1). <https://doi.org/10.1038/s41467-018-07690-0>
- Bruno, R., & Trenchi, L. (2014). Radial dependence of the frequency break between fluid and kinetic scales in the solar wind fluctuations. *The Astrophysical Journal*, 787(2), L24. <https://doi.org/10.1088/2041-8205/787/2/L24>
- Burch, J. L., Moore, T. E., Torbert, R. B., & Giles, B. L. (2016). Magnetospheric multiscale overview and science objectives. *Space Science Reviews*, 199(1–4), 5–21. <https://doi.org/10.1007/s11214-015-0164-9>
- Burkholder, B. L., & Otto, A. (2019). Magnetic Reconnection of solar flux tubes and coronal reconnection signatures in the solar wind at 1 AU. *Journal of Geophysical Research: Space Physics*, 124(11), 8227–8254. <https://doi.org/10.1029/2019JA027114>
- Chasapis, A., Matthaeus, W. H., Parashar, T. N., Fuselier, S. A., Maruca, B. A., Phan, T. D., et al. (2017). High-resolution statistics of solar wind turbulence at kinetic scales using the magnetospheric multiscale mission. *The Astrophysical Journal*, 844(1), L9. <https://doi.org/10.3847/2041-8213/aa7ddd>
- Chen, C. H. K., Leung, L., Boldyrev, S., Maruca, B. A., & Bale, S. (2014). Ion-scale spectral break of solar wind turbulence at high and low beta. *Geophysical Research Letters*, 41(22), 8081–8088. <https://doi.org/10.1002/2014GL062009>

- Farris, M. H., & Russell, C. T. (1994). Determining the standoff distance of the bow shock: Mach number dependence and use of models. *Journal of Geophysical Research: Space Physics*, 99(A9), 17681–17689. <https://doi.org/10.1029/94JA01020>
- FPI-Team. (2021). *MMS FPI data users and Products Guide*. Retrieved from <https://lasp.colorado.edu/galaxy/display/MFDPG/MMS+FPI+Data+Users+and+Products+Guide>
- Gershman, D. J., Avanov, L. A., Boardsen, S. A., Dorelli, J. C., Giessie, U., Barrie, A. C., et al. (2017). Spacecraft and Instrument Photoelectrons Measured by the Dual Electron Spectrometers on MMS. *Journal of Geophysical Research: Space Physics*, 122(11), 11,548–11,558. <https://doi.org/10.1002/2017JA024518>
- Gershman, D. J., Dorelli, J. C., F. Viñas, A., & Pollock, C. J. (2015). The calculation of moment uncertainties from velocity distribution functions with random errors. *Journal of Geophysical Research: Space Physics*, 120(8), 6633–6645. <https://doi.org/10.1002/2014JA020775>
- Halekas, J. S., Poppe, A. R., & McFadden, J. P. (2014). The effects of solar wind velocity distributions on the refilling of the lunar wake: ARTEMIS observations and comparisons to one-dimensional theory. *Journal of Geophysical Research: Space Physics*, 119(7), 5133–5149. <https://doi.org/10.1002/2014JA020083>
- Harten, R., & Clark, K. (1995). The design features of the GGS wind and polar spacecraft. *Space Science Reviews*, 71, 23–40. <https://doi.org/10.1007/BF00751324>
- King, J. H., & Papitashvili, N. (2005). Solar wind spatial scales in and comparisons of hourly Wind and ACE plasma and magnetic field data. *Journal of Geophysical Research*, 110(A2), A02104. <https://doi.org/10.1029/2004JA010649>
- Koskinen, H. E. J. (2002). Magnetospheric energy budget and the epsilon parameter. *Journal of Geophysical Research*, 107(A11), 1415. <https://doi.org/10.1029/2002JA009283>
- Lavraud, B., & Larson, D. E. (2016). Correcting moments of in situ particle distribution functions for spacecraftelectrostatic charging. *Journal of Geophysical Research: Space Physics*, 121, 8462–8474. <https://doi.org/10.1002/2016JA022591>
- Leamon, R. J., Smith, C. W., Ness, N. F., Matthaeus, W. H., & Wong, H. K. (1998). Observational constraints on the dynamics of the interplanetary magnetic field dissipation range. *Journal of Geophysical Research: Space Physics*, 103(A3), 4775–4787. <https://doi.org/10.1029/97JA03394>
- Lepping, R. P., Acuña, M. H., Burlaga, L. F., Farrell, W. M., Slavin, J. A., Schatten, K. H., & Worley, E. M. (1995). The Wind magnetic field investigation. *Space Science Reviews*, 71(1–4), 207–229. <https://doi.org/10.1007/BF00751330>
- Markovskii, S. A., Vasquez, B. J., & Smith, C. W. (2008). Statistical analysis of the high-frequency spectral break of the solar wind turbulence at 1 AU. *The Astrophysical Journal*, 675(2), 1576–1583. <https://doi.org/10.1086/527431>
- McFadden, J. P., Carlson, C. W., Larson, D., Bonnell, J., Mozer, F., Angelopoulos, V., et al. (2008a). THEMIS ESA first science results and performance issues. In *The Themis mission* (pp. 277–302). New York, NY: Springer New York. <https://doi.org/10.1007/s11214-008-9433-1>
- McFadden, J. P., Carlson, C. W., Larson, D., Bonnell, J., Mozer, F., Angelopoulos, V., et al. (2008b). THEMIS ESA first science results and performance issues. *Space Science Reviews*, 141, 477–508. <https://doi.org/10.1007/s11214-008-9433-1>
- McFadden, J. P., Carlson, C. W., Larson, D., Ludlam, M., Abiad, R., Elliott, B., & Angelopoulos, V. (2008). The THEMIS ESA plasma instrument and in-flight calibration. In *The themis mission* (pp. 277–302). New York, NY: Springer New York. [https://doi.org/10.1007/978-0-387-89820-9\\_13](https://doi.org/10.1007/978-0-387-89820-9_13)
- Ogilvie, K., & Desch, M. (1997). The Wind spacecraft and its early scientific results. *Advances in Space Research*, 20(4–5), 559–568. [https://doi.org/10.1016/S0273-1177\(97\)00439-0](https://doi.org/10.1016/S0273-1177(97)00439-0)
- Ogilvie, K. W., Chornay, D. J., Fritzenreiter, R. J., Hunsaker, F., Keller, J., Lobell, J., & Gergin, E. (1995). SWE, a comprehensive plasma instrument for the Wind spacecraft. *Space Science Reviews*, 71(1–4), 55–77. <https://doi.org/10.1007/BF00751326>
- Padhye, N. S., Smith, C. W., & Matthaeus, W. H. (2001). Distribution of magnetic field components in the solar wind plasma. *Journal of Geophysical Research: Space Physics*, 106(A9), 18635–18650. <https://doi.org/10.1029/2000ja000293>
- Paschmann, G., Fazakerley, A. N., & Schwartz, S. (2000). Moments of plasma velocity distributions. In *Analysis methods for multi-spacecraft data* (pp. 125–158).
- Pollock, C., Moore, T., Jacques, A., Burch, J., Giessie, U., Saito, Y., et al. (2016). Fast plasma investigation for magnetospheric multiscale. *Space Science Reviews*, 199(1–4), 331–406. <https://doi.org/10.1007/s11214-016-0245-4>
- Roberts, O. W., Nakamura, R., Torkar, K., Narita, Y., Holmes, J. C., Vörös, Z., et al. (2020). Sub-ion scale compressive turbulence in the solar wind: MMS spacecraft potential observations. *The Astrophysical Journal - Supplement Series*, 250(2), 35. <https://doi.org/10.3847/1538-4365/ab45d>
- Roberts, O. W., Narita, Y., Li, X., Escoubet, C. P., & Laakso, H. (2017). Multipoint analysis of compressive fluctuations in the fast and slow solar wind. *Journal of Geophysical Research: Space Physics*, 122(7), 6940–6963. <https://doi.org/10.1002/2016JA023552>
- Russell, C. T., Anderson, B. J., Baumjohann, W., Bromund, K. R., Dearborn, D., Fischer, D., & Richter, I. (2016). The magnetospheric multiscale magnetometers. *Space Science Reviews*, 199(1–4), 189–256. <https://doi.org/10.1007/s11214-014-0057-3>
- Stone, E., Frandsen, A. M., Mewaldt, R., Christian, E., Margolies, D., Ormes, J., & Snow, F. (1998). The advanced composition explorer. *Space Science Reviews*, 86, 1–22. <https://doi.org/10.1023/A:1005082526237>
- Torkar, K., Nakamura, R., Tajmar, M., Scharlemann, C., Jeszenszky, H., Laky, G., et al. (2016). Active spacecraft potential control investigation. *Space Science Reviews*, 199(1–4), 515–544. <https://doi.org/10.1007/s11214-014-0049-3>
- Turc, L., Fontaine, D. W., Savioni, P., Hietala, H., Battarbee, M., Brito, T., et al. (2013). A comparison of bow shock models with Cluster observations during low Alfvén Mach number magnetic clouds. *Annales Geophysicae*, 31, 1011–1019. <https://doi.org/10.5194/angeo-31-1011-2013>
- Turc, L., Roberts, O. W., Archer, M. O., Palmroth, M., Battarbee, M., Brito, T., et al. (2019). First observations of the disruption of the earth's foreshock wave field during magnetic clouds. *Geophysical Research Letters*, 46(22), 12644–12653. <https://doi.org/10.1029/2019GL084437>
- Vokhmyanin, M. V., Stepanov, N. A., & Sergeev, V. A. (2019). On the evaluation of data quality in the OMNI interplanetary magnetic field database. *Space Weather*, 17, 476–486. <https://doi.org/10.1029/2018SW002113>
- Wilson III, L. B., Brosius, A. L., Gopalswamy, N. , Nieves-Chinchilla, T. , Szabo, A. , Hurley, K., et al. (2021). A quarter century of wind spacecraft discoveries. *Reviews of Geophysics*, 59, e2020RG000714. <https://doi.org/10.1029/2020rg000714>
- Wilson III, L. B., Sibeck, D. G., Breneman, A. W., Le Contel, O., Cully, C., Turner, D. L., et al. (2014). Quantified energy dissipation rates in the ter-restrial bow shock: 1. Analysis techniques and methodology. *Journal of Geophysical Research: Space Physics*, 119, 6455–6474. <https://doi.org/10.1002/2014JA019929>
- Wilson III, L. B., Stevens, M. L., Kasper, J. C., Klein, K. G., Maruca, B. A., Bale, S. D., et al. (2018). The statistical properties of solar wind temperature parameters near 1 au. *The Astrophysical Journal - Supplement Series*, 236(2), 41. <https://doi.org/10.3847/1538-4365/aab71c>
- Young, D. T., Burch, J. L., Gomez, R. G., De Los Santos, A., Miller, G. P., Wilson, P., & Webster, J. M. (2016). Hot plasma composition analyzer for the magnetospheric multiscale mission. *Space Science Reviews*, 199(1–4), 407–470. <https://doi.org/10.1007/s11214-014-0119-6>